EXPERIMENTAL STUDY OF AXIAL SPACING EFFECTS ON STACKED ROTOR PERFORMANCE IN HOVER AND FORWARD FLIGHT

Paskal Magier
PhD candidate
Université de Sherbrooke
Sherbrooke, Québec, Canada

Matthieu David
Masters Student
École Centrale de Nantes
Nantes, France

Benjamin Maury
Masters Student
École Centrale de Nantes
Nantes, France

Hachimi Fellouah
Professor
Université de Sherbrooke
Sherbrooke, Québec, Canada

ABSTRACT

The dual co-rotating coaxial rotor, referred to as a stacked rotor, is an unconventional configuration featuring blades arranged in multiple planes with unequal azimuthal spacing. This study presents an experimental investigation of a 0.82 m diameter stacked rotor operating at a constant rotational speed of 2468 RPM. The aim is to assess the effects of azimuthal spacing and axial spacing on system performance in terms of blade and power loading. Azimuthal spacing was varied across the full range, with finer resolution near blade overlap (0°), and two dimensionless axial spacings were tested: a smaller value of 0.06 and a larger value of 0.115. In hover, the larger axial spacing consistently outperformed the smaller one in blade loading and power loading, while showing reduced sensitivity to azimuthal spacing due to weaker aerodynamic interference between rotors when azimuthal spacing is varied. Compared to the baseline single rotor, the larger spacing exceeded its performance across all azimuthal spacings, whereas the smaller spacing exhibited a low-performance region near blade overlap. In forward flight, the percentage change in blade loading relative to the baseline generally decreased compared to hover, yet remained notably positive near an azimuthal spacing of ±90°. However, this configuration typically generated greater drag than the baseline in that region, while the aerodynamic balance shifted in favor of the stacked rotor, producing less drag and higher power loading, when azimuthal spacing approached 0°. Although the rotor was not trimmed for lift or propulsive force, the results indicate that in forward flight, larger axial spacing can match baseline performance when blades are closely aligned in azimuth, whereas smaller spacings perform better at larger azimuthal separations.

NOTATION

C_H	Rotor drag force coefficient
C_Y	Rotor side force coefficient
C_T	Rotor thrust coefficient
C_{M_x}	Rotor rolling moment coefficient
C_{M_y}	Rotor pitching moment coefficient
C_P	Rotor power coefficient
C_D	Drag coefficient
$F_{x,y,z}$	Forces measured along x,y,z-axis
R	Rotor radius
$T_{x,y,z}$	Torques measured along x,y,z-axis
u_t	Total uncertainty
U_∞	Freestream velocity
α_s	Shaft angle
Δz	Axial spacing between upper and lower rotor
Ω	Rotor rotational speed
ϕ	Azimuthal spacing
σ_{sr}	Solidity of a single two-bladed rotor
σ	Total rotor solidity, $2\sigma_{sr}$

INTRODUCTION

Urban Air Mobility (UAM) aims to provide rapid transportation in densely populated areas while avoiding ground traffic congestion. The emergence of electric Vertical Take-Off and Landing (eVTOL) aircraft, enabled by advances in electric powertrains, battery technology, and Distributed Electric Propulsion (DEP), has revived interest in unconventional rotor configurations. Among these, the co-rotating coaxial or stacked rotor, characterized by blades arranged in multi-

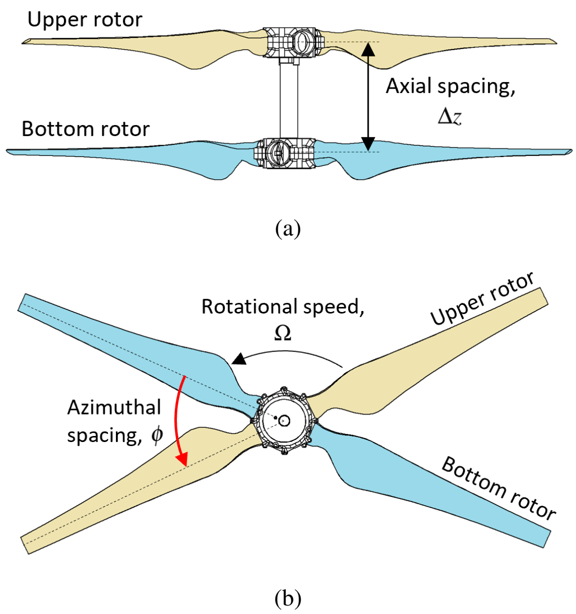

Figure 1: (a) axial spacing (b) azimuthal spacing of a stacked rotor configuration

ple planes with unequal azimuthal spacing, as seen in Figure 1, offers a promising combination of compactness, performance potential, and noise reduction capability. DEP facilitates multirotor designs that are easier to torque-balance, and the stacked rotor has reemerged in the past decade as an alternative to contra-rotating coaxial systems. Early studies have shown that certain stacked rotor configurations can outperform conventional single rotors and, in specific cases, rival contra-rotating coaxial rotors.

The stacked rotor concept was first investigated in the 1970s for potential military applications, such as reducing tail rotor acoustic signatures (Refs. 1–3). Interest resurfaced in the early 2010s, driven by findings that the performance advantages of contra-rotating coaxial rotors were not solely attributable to swirl recovery (Ref. 4). The flexibility to vary axial spacing, azimuthal spacing, differential blade collective pitch, blade tip speed, rotor radius, and blade geometry opens a vast design space that directly influences both aerodynamic and aeroacoustic behavior.

Stacked rotor aerodynamics have been widely examined, primarily in hover flight, revealing the strong influence of axial and azimuthal spacings (Refs. 1, 5–15), as well as the effects of differential collective pitch (Refs. 1, 5, 14), rotor radius (Refs. 1, 14), tip speed (Ref. 9), and blade geometry (Refs. 16,17). Across these studies, three key aerodynamic mechanisms emerge. First, airfoil interaction occurs between the bound circulations of the upper and lower rotors, becoming especially pronounced when blades pass in close proximity (Refs. 13, 16). Second, inflow effects raise the velocity at the lower rotor disk due to the downward-accelerated wake of the upper rotor (Refs. 1, 18–21). Third, under certain configurations, blade–vortex interaction arises when the tip vortices shed by the upper rotor intersect with the blades of the lower rotor (Refs. 19–21). Together, these effects shape the aerodynamic loads on both rotors, defining a large and complex design space that governs both aerodynamic performance and aeroacoustic characteristics.

A recent study (Ref. 22) investigated forward flight performance at a small dimensionless axial spacing of $\Delta z/R = 0.06$. For various shaft angles α_s and freestream velocities U_∞, it was observed that the low-performance region relative to hover expanded around $\phi = 0°$, while regions where the stacked rotor outperformed the baseline were reduced and shifted toward $\phi \approx \pm 90°$. Vibratory load measurements revealed that azimuthal spacing strongly affected hub moments: $\phi = 0°$ produced a dominant two-per-revolution harmonic, whereas $\phi = 90°$ yielded a four-per-revolution harmonic. Overall, the stacked rotor transmitted higher vibratory loads to the hub than the four-bladed baseline rotor.

The present work extends that study by refining the analysis of azimuthal spacing effects within the blade-overlap range and examining the influence of axial spacing. Two values are considered: a small spacing of $\Delta z/R = 0.06$, where previous results have shown that aerodynamic interference is significant, and a larger spacing of $\Delta z/R = 0.115$, expected to reduce such interactions. The paper first presents the baseline rotor performance in forward flight, followed by stacked rotor performance in hover, and concludes with a forward flight comparison between the baseline and stacked rotor configurations.

METHODOLOGY

The methodology is organized as follows. First, the experimental setup and its installation in the wind tunnel are described, along with the adjustable parameters and achievable configurations. This is followed by an overview of the measurement and control systems, the test matrix, and the data acquisition procedure. Finally, the uncertainty estimation for the load cell is presented, together with the post-processing approach used to define the variables of interest analyzed in this study.

Experimental setup

The experimental campaign was conducted in a closed-circuit, low-speed wind tunnel at the Université de Sherbrooke (Québec, Canada). The 10-meter-long (33-foot) test section has a square cross-section of 1.82 by 1.82 square meters (6 by 6 square feet), with uniform streamwise velocity within ±0.3% and turbulence intensity below 0.5%. Boundary layers near the walls are about 5 centimeters (2 inches) thick. The stacked rotor rig was positioned approximately 0.5 m (20 inches) from all walls to limit wall effects. A depiction of the experimental setup installed in the wind tunnel, shown in axial flight mode, can be found in Figure 2.

The system consists of two identical rotors fitted with KDE-CF305 carbon fiber blades (highly twisted, tapered), with a measured blade mass imbalance below 0.25 g per rotor. Rigid rotor hubs are considered in this study to eliminate flapping

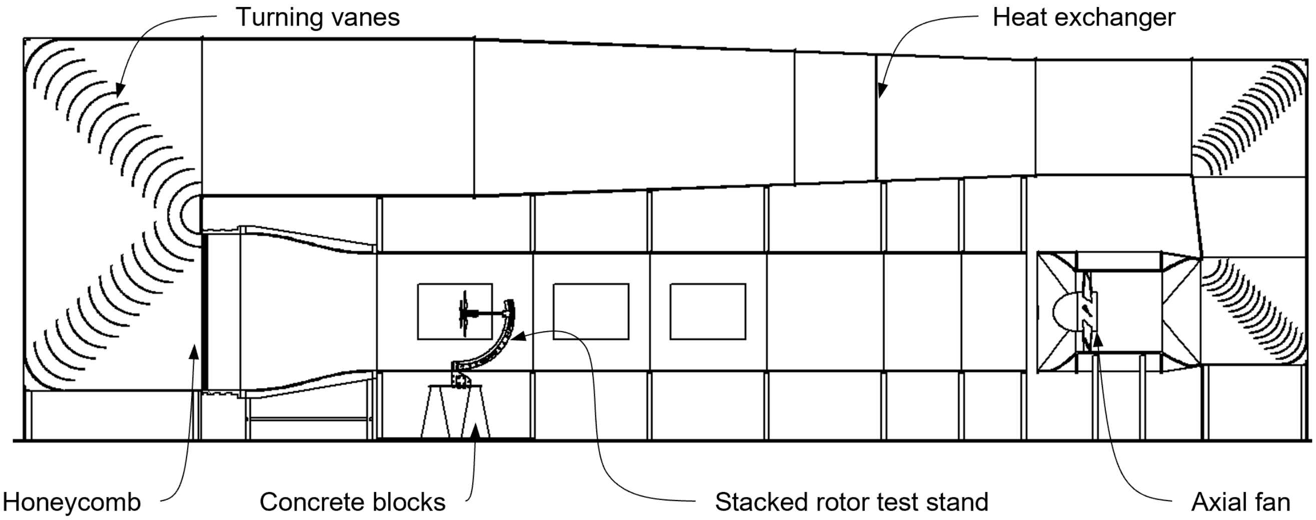

Figure 2: Cutaway view of the experimental setup in axial flight mode inside the wind tunnel

and lead–lag motion. The rotor diameter, including the hub, is $D = 0.8183$ m (32.2 inches), with a root cut-out of 16.33%R. The single-rotor solidity, based on the 75%R chord, is $\sigma_{sr} = 0.074$.

A modular "C-shaped" support holds the shaft in either axial or forward flight configurations as shown in Figure 3. In both cases, the rotor disk plane is placed at least two rotor radii away from structural elements to minimize interference effects (Refs. 23, 24). In forward flight, a shorter support reduces vibration and improves rigidity.

Parameter adjustments

Dimensionless axial spacing ($\Delta z/R$) is set by interchangeable spacers mounted on a grooved, threaded shaft. Continuous adjustment between 0.06 and 0.15 is possible without blade or hub interference. At $\Delta z/R = 0$ and $\phi = 90°$, the system forms a baseline four-bladed rotor.

Azimuthal spacing (ϕ) is adjusted via an index plate with 120 teeth (3° increments), combined with offset hole patterns allowing 1° resolution. Machining tolerances limit ϕ uncertainty to 0.4°.

Shaft angle (α_s) is varied in ±30° range in 2.5° increments, with a tolerance of 0.03°.

Figure 4 presents a close-up view of the experimental setup in forward flight mode, highlighting the axial spacing and shaft angle adjustment mechanisms, while Figure 5 shows an exploded view of the rotor shaft, illustrating the azimuthal spacing adjustment mechanism.

Measurement and control systems

The test stand is powered by a KDE Direct 8218XF-120 BLDC motor, driven by a RoboteQ GBLG2660TS controller and supplied by a 5 kW TDK-Lambda GEN 40-125 DC source. Hall sensors in the motor provide feedback to the controller for closed-loop rotation rate control, while an RM08 magnetic encoder (4096 pulse-per-revolution) from RLS mounted on the shaft measures the actual rotor speed with higher accuracy. This enables precise monitoring of the real rotation rate, with a measured standard deviation of $\sigma_\Omega = 0.38$ RPM over all tests in this paper.

Table 1: ATI Delta SI-660-60 features

	Sensing range	Resolution	Uncertainty (% of FS[a] load)
Fx, Fy	660 N	1/8 N	1.25
Fz	1980 N	1/4 N	1.5
Tx	60 Nm	10/1333 Nm	1
Ty	60 Nm	10/1333 Nm	1.25
Tz	60 Nm	10/1333 Nm	1.75

[a]FS: full-scale

Loads are measured with an ATI Delta SI-660-60 six-component force transducer, whose sensing range, resolution, and manufacturer-stated uncertainties are listed in Table 1. Previous studies (Refs. 9, 10, 25) have reported thermal drift when such load cells are mounted near electric motors. To limit this effect, a polyoxymethylene (POM) thermal isolator is installed between the motor and the transducer, with a thermocouple monitoring the load cell temperature. All signals are acquired synchronously on a National Instruments PCIe-6363 DAQ at 22 kHz using a LabVIEW interface.

Test matrix and procedure

The primary test variables are shaft angle α_s, freestream velocity U_∞, azimuthal spacing ϕ, and axial spacing $\Delta z/R$. Two axial spacings are tested: $\Delta z/R = 0.06$ and $\Delta z/R = 0.115$. Shaft angle is varied from 0° to 30° in 5° increments, and freestream velocity from 5 to 20 m.s^{-1} in 5 m.s^{-1} incre-

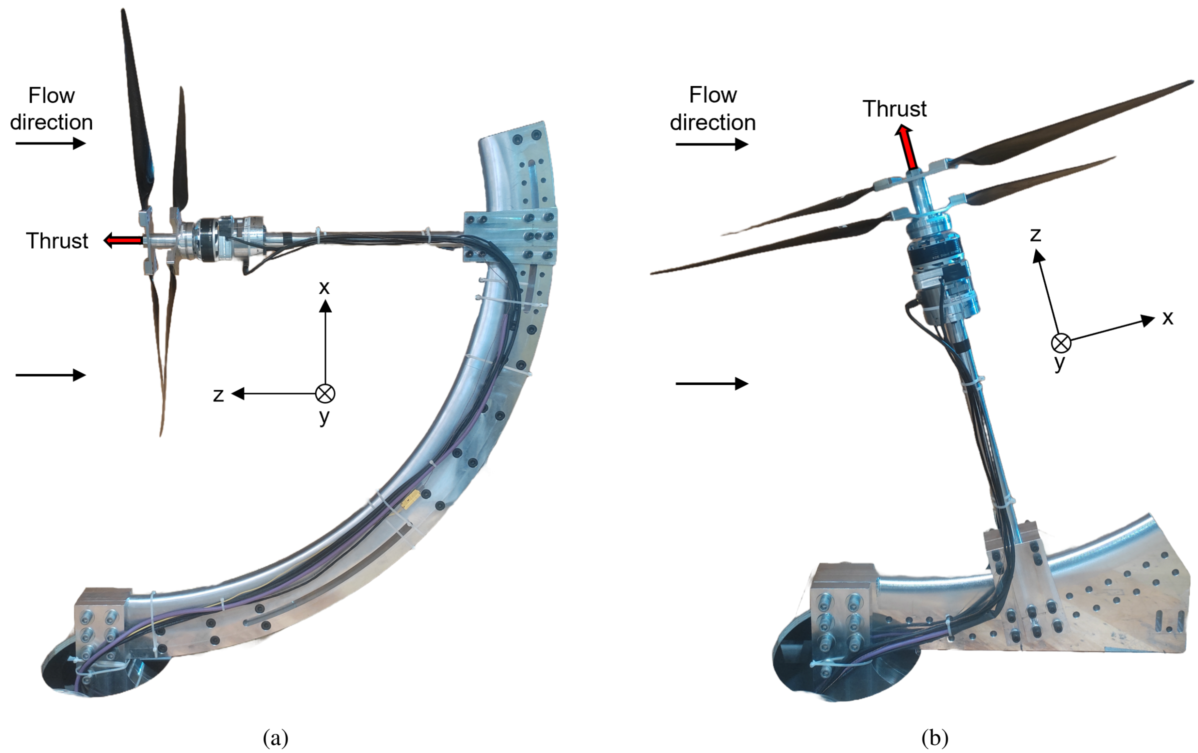

Figure 3: Experimental setup in (a) axial flight mode, α_s = 90° (b) forward flight mode, α_s = 15°

ments. Azimuthal spacing is varied from −75° to 90°, with 3° increments between −15° and 15°, and 15° increments elsewhere (note that for the 2 × two-bladed configuration, $\phi = -90°$ is identical to $\phi = 90°$). Rotational speed is held at $\Omega = 2468$ RPM, corresponding to tip Mach numbers from 0.25 (retreating side, $\alpha_s = 0°$, U_∞ = 20 m/s) to 0.37 (advancing side, same conditions). The chord-based Reynolds number ranges from 2.8×10^5 to 4.12×10^5, within the low-Reynolds regime where transitional effects may impact performance (Ref. 26).

In hover tests ($\alpha_s = 90°$, $U_\infty = 0$ m.s^{-1}), recirculation from the closed-circuit wind tunnel is mitigated with a deviation tarp installed 10 rotor diameters downstream. The baseline single four-bladed rotor configuration ($\Delta z/R = 0$, $\phi = 90°$) is also tested for each α_s and U_∞. In total, 1218 tests are performed, with forces and moments recorded for 200 revolutions at 22 kHz. A summary of conditions is provided in Table 2.

Table 2: Test matrix (configuration tested indicated by a ×) For each case, the baseline rotor is tested, along with all azimuthal spacings for the stacked rotor system from $\phi = -75°$ to 90°, using 3° increments between −15° and 15° and 15° increments elsewhere. Two axial spacings are considered: $\Delta z/R = 0.06$ and $\Delta z/R = 0.115$.

		U_∞ (m.s^{-1})				
		0	5	10	15	20
α_s	0°		×	×	×	×
	5°		×	×	×	×
	10°		×	×	×	×
	15°		×	×	×	×
	20°		×	×	×	×
	25°		×	×	×	×
	30°		×	×	×	×
	90°	×				

Uncertainty estimation

The manufacturer-stated uncertainties of the load cell (Table 1) are expressed as a percentage of the full-scale load. For small force measurements, this value is assumed to be exaggerated.

The total measurement uncertainty, u_t, is evaluated by combining four sources: bias (u_b), hysteresis (u_h), precision (u_p), and drift (u_d). Bias and hysteresis, inherent to the device, were determined by applying known loads to each axis and comparing the measured and applied values. Eight load cases per axis were tested, covering ranges of −222 to 222 N (forces) and −11.1 to 11.1 Nm (moments), with the maximum absolute errors taken as u_b and u_h (Table 3).

The precision uncertainty, u_p, was computed from the standard deviation of the averaged loads over 200 rotor revolutions for each test case, assuming a normal distribution at a 95% confidence level.

Thermal drift, u_d, was estimated from the residual offset between initial and final static points after each test, most notable in the z-direction force (up to 2 N). A 5-minute pause was maintained before each test to stabilize the load cell temperature at approximately 35°C.

Finally, u_t was obtained using Equation 1, combining all four

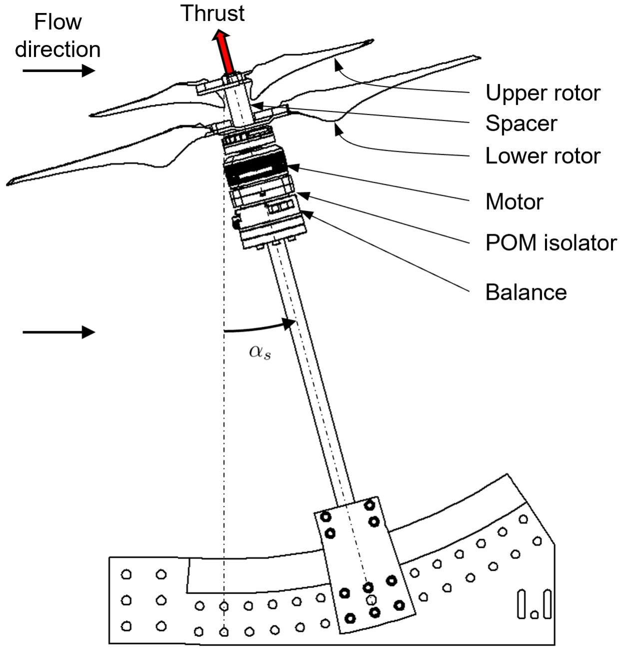

Figure 4: Close-up view of the experimental setup in forward flight mode

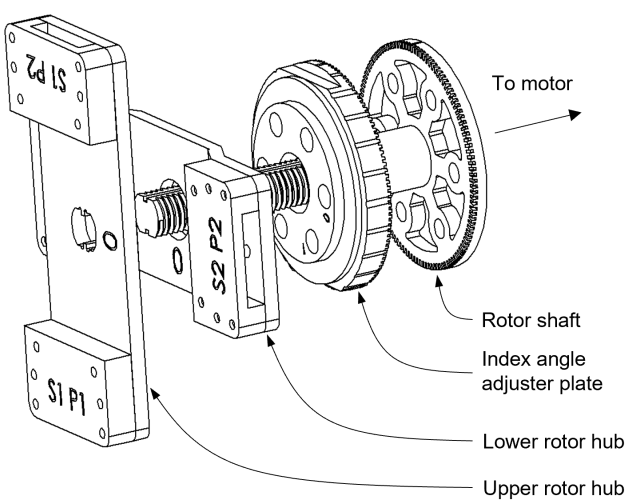

Figure 5: Exploded view of the rotor shaft

Table 3: Bias and hysteresis uncertainties of the load cell

	Bias uncertainty	Hysteresis uncertainty
Fx	2.246 N	0.107 N
Fy	2.078 N	0.151 N
Fz	0.823 N	0.302 N
Tx	0.251 Nm	0.004 Nm
Ty	0.255 Nm	0.037 Nm
Tz	0.269 Nm	0.008 Nm

sources.

$$u_t = \sqrt{u_b^2 + u_h^2 + u_p^2 + u_d^2} \quad (1)$$

Data processing apparatus

Encoder pulses identify each revolution. Because the acquisition rate and rotor speed are not harmonically matched, the instantaneous loads are linearly resampled onto a uniform azimuthal grid, enabling direct phase-averaging across revolutions.

Loads F_x, F_y, F_z, T_x, T_y, and T_z are measured in the load cell frame, located below the rotor reference frame. A correction for the axial offset between the load cell and the lower rotor disk transforms these measurements to the rotor frame, from which rotor drag H (x, downstream), side force Y (y, right), thrust T (z, up), rolling moment M_x (x, roll left), pitching moment M_y (y, nose up), and torque Q (z, nose left) are obtained, with axis orientation shown in Figure 3.

Dimensionless coefficients are then computed for each case using Equations 2–7, with ρ the air density, A the rotor disk area, Ω the rotor speed, and R the rotor radius.

$$C_H = \frac{H}{\rho A(\Omega R)^2} \quad (2)$$

$$C_Y = \frac{Y}{\rho A(\Omega R)^2} \quad (3)$$

$$C_T = \frac{T}{\rho A(\Omega R)^2} \quad (4)$$

$$C_{M_x} = \frac{M_x}{\rho A(\Omega R)^2 R} \quad (5)$$

$$C_{M_y} = \frac{M_y}{\rho A(\Omega R)^2 R} \quad (6)$$

$$C_Q = C_P = \frac{Q}{\rho A(\Omega R)^2 R} \quad (7)$$

The blade loading coefficient C_T/σ (Eq. 8) assesses rotor solidity effects and enables comparison between stacked and single (2-bladed) rotors. The power loading coefficient (Eq. 9) serves as a metric of rotor efficiency.

$$C_T/\sigma = \frac{T}{\rho A(\Omega R)^2 2\sigma_{sr}} \quad (8)$$

$$C_T/C_P = \frac{T\Omega R}{P} \quad (9)$$

RESULTS

The complete test matrix is summarized in Table 2. All experiments were performed at a fixed rotational speed of $\Omega = 2468$ RPM using two axial spacings, $\Delta z/R = 0.06$ and $\Delta z/R = 0.115$, for the stacked rotor configuration. The influence of shaft angle α_s, freestream velocity U_∞, and azimuthal spacing ϕ is examined in the following sections. The results begin with the baseline rotor (a single four-bladed rotor, $\Delta z/R = 0$, $\phi = 90°$) in forward flight, followed by hover results for the stacked system, and finally forward flight results for the stacked configuration.

In forward flight, a shaft tilt angle α_s splits rotor thrust into a vertical lift component and a horizontal propulsive component. In the rotor frame, the freestream velocity U_∞ decomposes into an axial component $U_\infty \sin\alpha_s$ and an in-plane component $U_\infty \cos\alpha_s$, producing asymmetric inflow across the disk and unsteady aerodynamic loads.

Baseline rotor in forward flight

Figure 6 presents the baseline rotor performance as a function of U_∞ and α_s, based on raw time-averaged measurements (no smoothing or interpolation).

In the blade loading contours (Figure 6a), a clear trend emerges. For small shaft angles ($\alpha_s < 20°$), blade loading increases as freestream velocity rises. In contrast, when the shaft angle is large ($\alpha_s > 20°$), blade loading decreases with increasing freestream velocity. In general, blade loading levels are higher at lower shaft angles.

These trends can be explained by decomposing the freestream velocity into two components relative to the rotor disk: the axial component $U_\infty \sin\alpha_s$ and the in-plane component $U_\infty \cos\alpha_s$. The axial component acts as an additional inflow through the disk, increasing downwash and reducing the blades' angle of attack, which in turn lowers thrust. The in-plane component, however, produces asymmetric loading between the advancing and retreating sides of the rotor. On the advancing side, blade motion adds to the freestream velocity, increasing relative airspeed and generating more lift; on the retreating side, the opposite occurs. Because lift grows with the square of relative velocity, the net effect of this asymmetry is a thrust gain.

At small shaft angles, the in-plane component is dominant, so the overall effect of increasing freestream velocity is an increase in blade loading. At high shaft angles, the axial component becomes dominant, and its thrust-reducing influence outweighs the asymmetric lift gain from the in-plane component, causing blade loading to decrease with velocity.

The power loading trends in Figure 6b mirror those of blade loading. With the baseline rotor not trimmed for lift or propulsive force, input power remains nearly constant ($C_P = 1.33 \times 10^{-3}$, $\sigma_{C_P} = 3.65 \times 10^{-5}$), meaning changes in power loading primarily reflect thrust variations.

Figures 6c and 6d show rolling (M_x) and pitching (M_y) moments. Lift imbalances across the disk produce these moments, which are transmitted directly to the rigid rotor hub. For the counterclockwise rotor, greater lift on the advancing side generates a positive (to the left) rolling moment.

Gyroscopic precession converts part of this lift asymmetry into a nose-up pitching moment, which grows with rotor speed due to increasing angular momentum. However, when the rotor is tilted, forward thrust also develops, corresponding to the horizontal projection of thrust minus rotor drag. For $\alpha_s > 5°$ this forward thrust is positive and introduces a negative pitching moment, partially offsetting the gyroscopic contribution.

Rolling moment depends mainly on U_∞, increasing as lift imbalance grows. Pitching moment depends on both U_∞ and α_s, with higher velocities and lower shaft angles yielding stronger nose-up moments.

Stacked rotor system in hover flight

In this study, two axial spacings were tested, $\Delta z/R = 0.06$ and $\Delta z/R = 0.115$, at a constant rotational speed of $\Omega = 2468$ RPM. In hover flight, with freestream velocity $U_\infty = 0$ m.s^{-1} and shaft angle $\alpha_s = 90°$, only the azimuthal spacing ϕ was varied. The azimuthal spacing, often called the index angle in the literature, represents the angular offset between the blades of the upper and lower rotors. Following a common convention, ϕ is considered positive when the upper rotor blade leads and negative when it lags.

Measurements were taken over a range from $\phi = -75°$ to $\phi = 90°$, with 3° increments between −15° and 15°, and 15° increments elsewhere. Since the configurations at $\phi = -90°$ and $\phi = 90°$ are equivalent, the latter is duplicated in the figures to center the graphs at $\phi = 0°$.

The total rotor blade loading as a function of azimuthal spacing for both axial spacings is shown in Figure 7a. The results follow trends well documented in the literature (Refs. 1, 6, 7, 11–14): performance is reduced near $\phi = 0°$ and improves at larger positive or negative spacings. Around $\phi = 0°$, the proximity of the blades amplifies pressure effects from the Venturi effect between overlapping sections, lowering performance for the upper rotor while enhancing it for the lower (Refs. 11, 16). Additional airfoil interaction effects in this region can produce the minimum total thrust when the lower rotor slightly leads (Refs. 11, 13, 16). In previous experiments (Ref. 22), this reduction was not captured due to coarse azimuthal spacing increments, a limitation overcome in the present study by employing finer resolution near $\phi = 0°$.

When the individual rotor's thrusts are measured (Ref. 13), the results exhibit a highly unequal thrust sharing between both rotors. It is observed that for small axial spacing, the leading rotor consistently contributes more to the total thrust, this is attributed to the airfoil interaction effects between both rotors. However, for higher axial spacing, less dependence of azimthal spacing is observed, leading to less influence of airfoil interactions, and more due to the induced inflow, leading to the upper rotor consistently outperforming the lower rotor (Refs. 11, 12, 15). Consequently, the total rotor thrust for higher axial spacing is less influenced by the azimuthal spacing variation. (Refs. 1, 11–13).

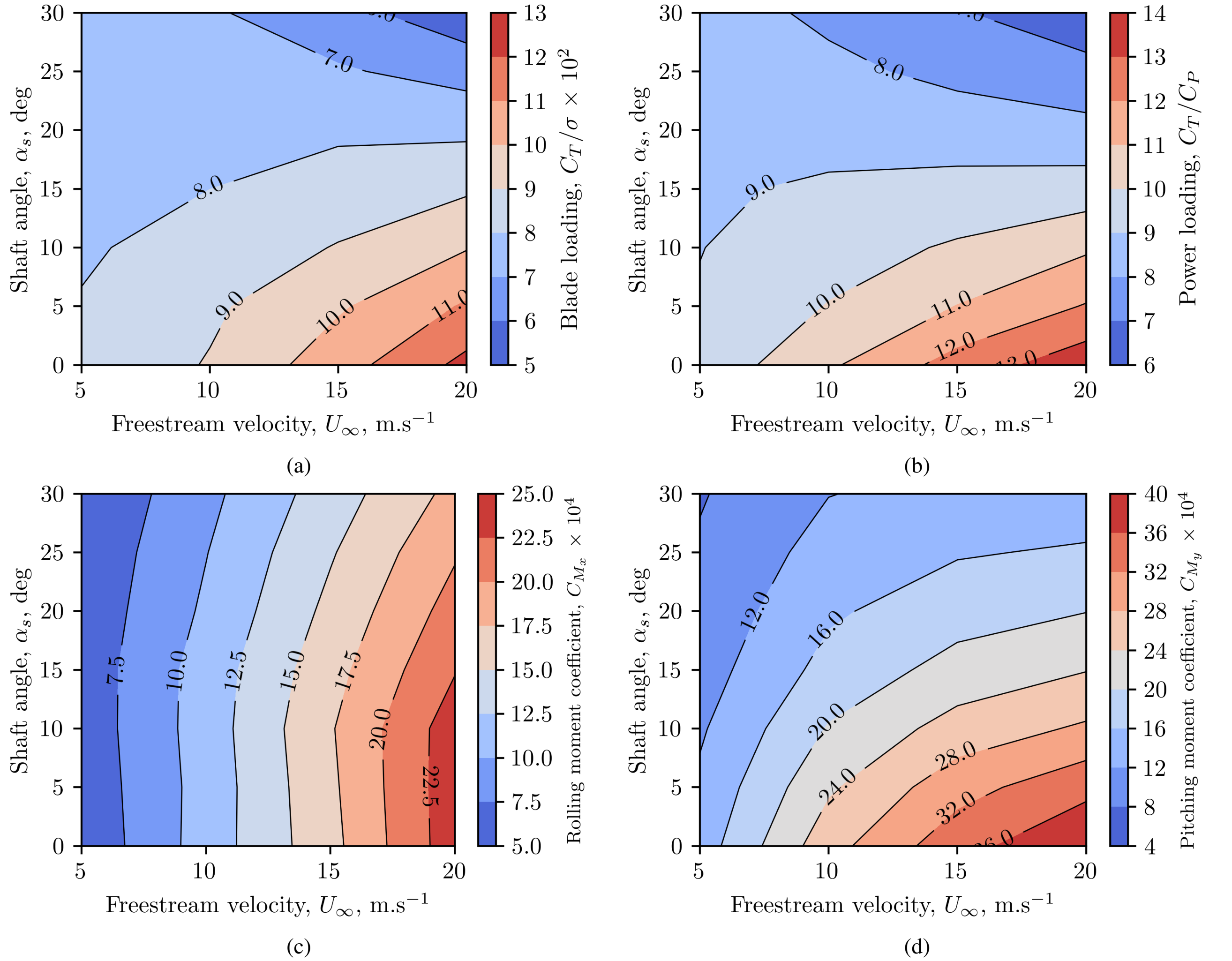

Figure 6: Baseline rotor configuration results versus shaft angles and freestream velocities. (a) Blade loading, $C_T/\sigma \times 10^2$ (b) Power loading, C_T/C_P (c) Rolling moment coefficient, $C_{M_x} \times 10^4$ (d) Pitching moment coefficient, $C_{M_y} \times 10^4$

This pattern is visible in Figure 7a, where a horizontal dotted line marks the baseline single-rotor blade loading ($C_T/\sigma = 7.72 \times 10^{-2}$). For $\Delta z/R = 0.115$, blade loading ranges from $C_T/\sigma = 7.85 \times 10^{-2}$ to 8.51×10^{-2}, while for $\Delta z/R = 0.06$, it ranges from 7.09×10^{-2} to 8.23×10^{-2}. This means the smaller spacing experiences nearly twice the variation between maximum and minimum values than the higher spacing. At $\Delta z/R = 0.06$, the peak corresponds to a $+6.61\%$ increase over baseline at $\phi = 75^\circ$, and the trough to a -8.15% change at $\phi = -3^\circ$. Except in the region between $\phi = -15^\circ$ and $\phi = 15^\circ$, all offsets yield higher performance than the baseline. For $\Delta z/R = 0.115$, all azimuthal spacings surpass the baseline, with a maximum increase of $+10.26\%$. Overall, the larger axial spacing consistently outperforms the smaller one. This is because the small spacing operates in a regime where airfoil interactions and induced inflow are both strong and highly coupled, whereas the larger spacing reduces both effects. As axial spacing increases further, the system approaches the performance of two isolated rotors, for which $C_T/\sigma = 9.98 \times 10^{-2}$, higher than that of a single four-bladed rotor ($C_T/\sigma = 7.72 \times 10^{-2}$) (Ref. 23).

The rotor power coefficient (Figure 7b) exhibits a similar trend: for $\Delta z/R = 0.06$, a minimum occurs at $\phi = -3^\circ$ with a -13.88% deviation from the baseline ($C_P = 1.39 \times 10^{-3}$), compared to -7.96% for $\Delta z/R = 0.115$. In both cases, power demand increases for larger positive and negative ϕ values but remains close to the baseline for most azimuthal spacings. Fluctuations in C_P are again smaller for the larger axial spacing.

Although the variation in measured power with ϕ is small relative to the overall uncertainty (particularly its main component, the bias uncertainty) the observed patterns are consistent. The load cell, selected to avoid saturation during forward flight, has a range oversized for hover conditions, which reduces sensitivity for power measurements (Ref. 22). Despite this, Figure 7c shows that power loading (C_T/C_P) exceeds the baseline value of $C_T/C_P = 8.28$ across all azimuthal spacings. For $\Delta z/R = 0.06$, near $\phi = 0^\circ$, the stacked rotor produces less thrust than the baseline, but the associated drop in power is proportionally greater, yielding higher power loading, with a weighted average of $C_T/C_P = 8.7$. At the larger axial spac-

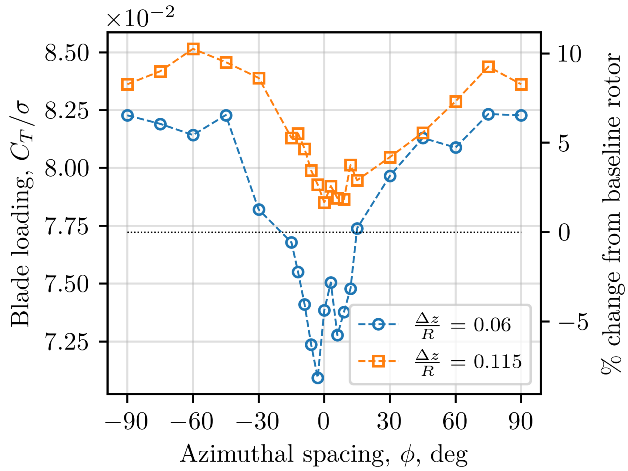

(a)

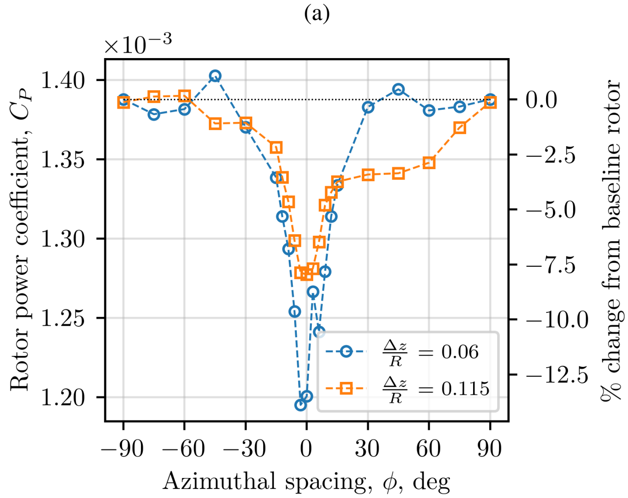

(b)

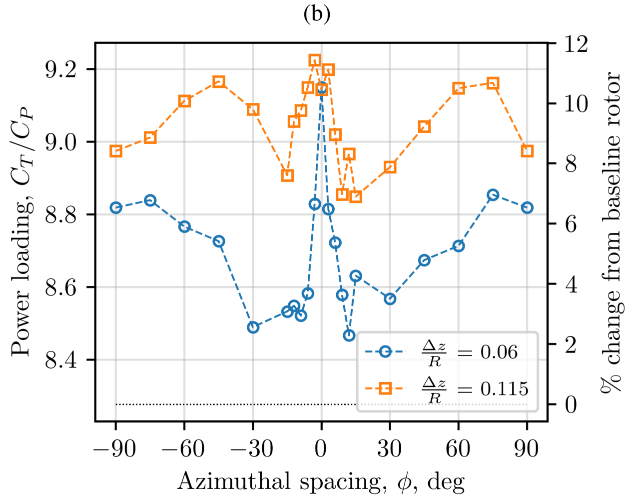

(c)

Figure 7: Hover flight results. Horizontal dotted lines represent the baseline rotor value. (a) Blade loading C_T/σ (b) Rotor power coefficient C_P (c) Power loading C_T/C_P

ing, $\Delta z/R = 0.115$, both thrust and power loading exceed the baseline, providing higher values than the smaller axial spacing, with a weighted average of $C_T/C_P = 9.03$, consistent with trends from previous studies (Refs. 11, 13).

Stacked rotor system in forward flight

In this section, the results for the stacked rotor system in forward flight are presented. As in hover flight, variations in the azimuthal spacing ϕ are examined, but here they are considered alongside changes in shaft angle α_s and freestream velocity U_∞, as in the analysis of the baseline rotor in forward flight. The performance is illustrated through Figures 8-15, which respectively display the blade loading C_T/σ, power loading C_T/C_P, and drag coefficient C_D. As for the baseline rotor results, these figures are based on contours constructed from time-averaged measurements without smoothing or interpolation.

Overall, the trends in performance variation with shaft angle and freestream velocity for the stacked rotor are similar to those observed for the baseline rotor (see Figure 6). Consequently, the stacked rotor results are presented as percentage changes relative to the baseline rotor values.

Figures 8–11 compare blade loading results for both axial spacings, showing trends generally similar to hover flight. In both cases, a region of reduced performance occurs near $\phi = 0°$, with increased performance in both positive and negative azimuthal spacing directions. However, unlike in hover flight, where most azimuthal spacings outperformed the baseline rotor, forward flight exhibits a larger extent of reduced performance. For $\Delta z/R = 0.06$, low-performance regions are much more prominent and grow with increasing freestream velocity, whereas for $\Delta z/R = 0.115$ such regions are narrower and more stable.

Higher performance regions in forward flight tend to occur near $\phi = \pm 90°$ for both axial spacings, and with increasing freestream velocity, these regions shift toward lower shaft angles. For high shaft angles ($\alpha_s > 20°$), performance relative to the baseline becomes negative across most of the azimuthal range for $\Delta z/R = 0.06$, while for $\Delta z/R = 0.115$ it remains negative over most—but not all—of the range. Previous literature (Ref. 22) has explained that at high shaft angles, the axial inflow component dominates the inflow distribution, reducing the skew angle χ of the upper rotor's wake and causing a greater portion of the lower rotor disk to operate in this wake. This mechanism is particularly visible at $\Delta z/R = 0.115$, where blade loading relative to the baseline is stable for moderate shaft angles (5–15°) but drops noticeably beyond 20°.

In earlier work (Ref. 22), the low-performance region was defined as $-30° \leq \phi \leq 30°$. Here, this range is narrowed to $-15° \leq \phi \leq 15°$ to facilitate comparison between the two axial spacings, since the higher axial spacing produces a narrower low-performance region. As in hover flight, this region corresponds to a region of higher power loading (Figures 12 and 13), resulting from reduced power requirements when rotor blades are closely aligned in azimuth. For $\Delta z/R =$

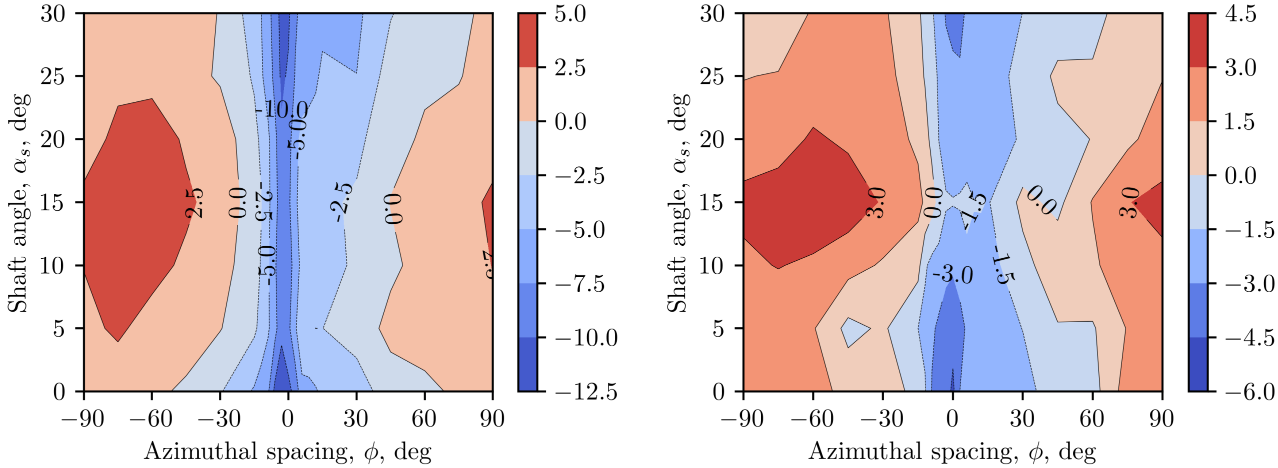

(a) (b)

Figure 8: Percentage change in blade loading C_T/σ relative to the baseline rotor value, plotted against azimuthal spacing ϕ and shaft angle α_s, for a freestream velocity of U_∞ = 5 m.s^{-1} and both axial spacings: (a) $\Delta z/R = 0.06$ (b) $\Delta z/R = 0.115$

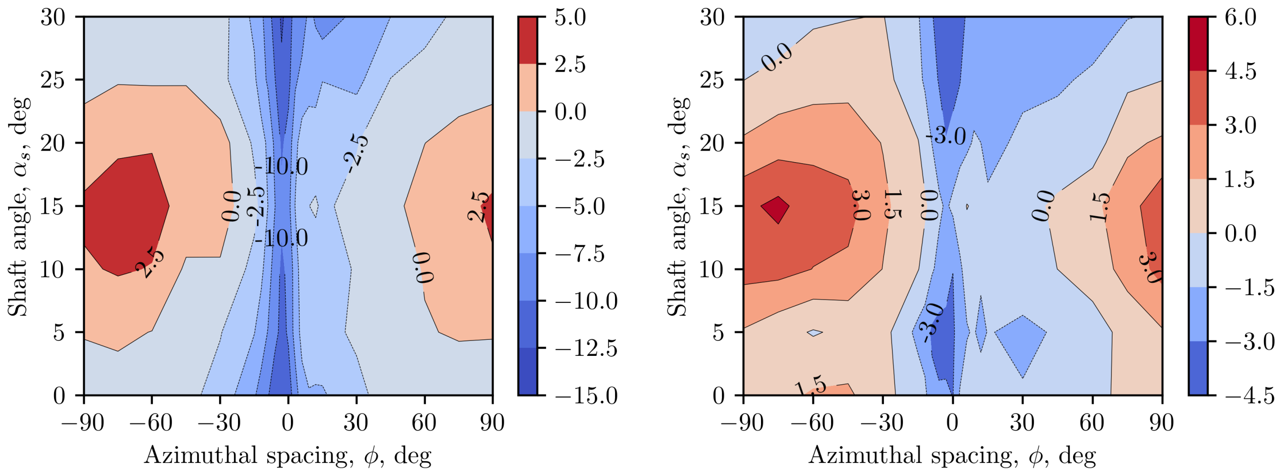

(a) (b)

Figure 9: Percentage change in blade loading C_T/σ relative to the baseline rotor value, plotted against azimuthal spacing ϕ and shaft angle α_s, for a freestream velocity of U_∞ = 10 m.s^{-1} and both axial spacings: (a) $\Delta z/R = 0.06$ (b) $\Delta z/R = 0.115$

0.06, power loading varies slightly around the baseline outside the low-performance region, with the largest differences confined within it. For $\Delta z/R = 0.115$, however, power loading is generally higher than the baseline, especially for $\alpha_s < 20°$, and the region of improved performance is larger across all U_∞ values.

Drag trends are shown in Figures 14 and 15 for two representative freestream velocities. Although coaxial rotors typically exhibit higher drag than single rotors, in co-rotative configurations this also depends on azimuthal spacing. When blades are closely aligned in the low-performance region, drag can drop below baseline values, while at $\phi \approx \pm 90°$ drag increases substantially. Increasing axial spacing to $\Delta z/R = 0.115$ amplifies the drag across most azimuthal spacings, though the low-performance region still exhibits a small drag reduction relative to the baseline.

Tables 4 and 5 summarize blade loading, power loading, and drag coefficient for both axial spacings and all freestream velocities, distinguishing between the low-performance region ($-15° \leq \phi \leq 15°$) and the rest of the azimuthal range. Outside the low-performance region, $\Delta z/R = 0.06$ yields slightly lower blade loading than $\Delta z/R = 0.115$, which performs comparably to the baseline rotor, contrasting with hover flight, where the higher axial spacing showed a substantial advantage. Power loading outside the low-performance region is generally higher for $\Delta z/R = 0.115$ than for $\Delta z/R = 0.06$, however, drag is also significantly greater, reaching an $+8.3\%$ increase at U_∞ = 5 m.s^{-1} and $+1.4\%$ at U_∞ = 20 m.s^{-1}.

Within the low-performance region, the smaller axial spacing performs notably worse than the larger one. For blade loading, $\Delta z/R = 0.115$ remains close to the baseline, while $\Delta z/R = 0.06$ is up to -7.3% lower. This pattern carries over to power loading, which fluctuates within $\pm 2\%$ of the base-

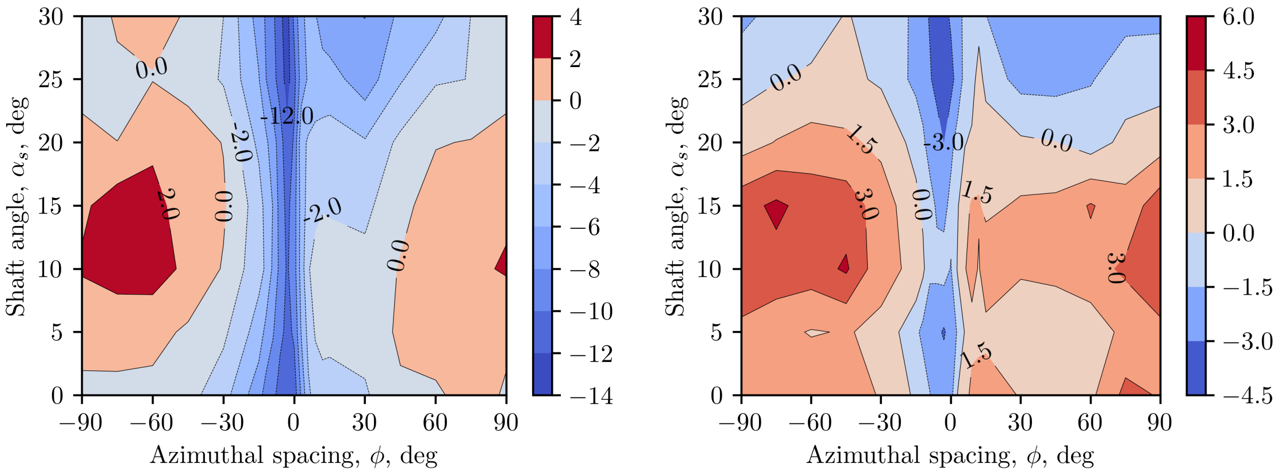

(a) (b)

Figure 10: Percentage change in blade loading C_T/σ relative to the baseline rotor value, plotted against azimuthal spacing ϕ and shaft angle α_s, for a freestream velocity of U_∞ = 15 m.s^{-1} and both axial spacings: (a) $\Delta z/R = 0.06$ (b) $\Delta z/R = 0.115$

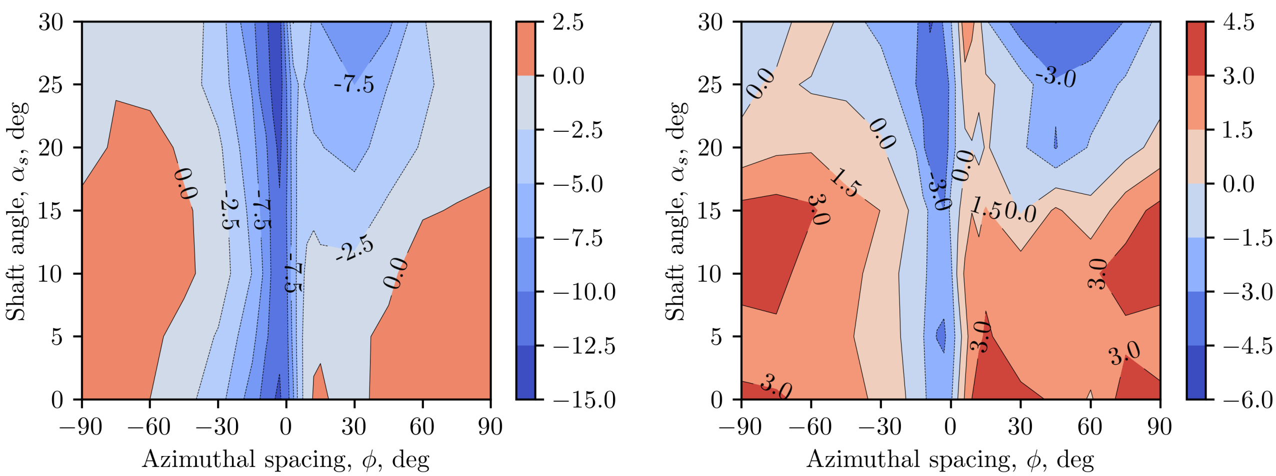

(a) (b)

Figure 11: Percentage change in blade loading C_T/σ relative to the baseline rotor value, plotted against azimuthal spacing ϕ and shaft angle α_s, for a freestream velocity of U_∞ = 20 m.s^{-1} and both axial spacings: (a) $\Delta z/R = 0.06$ (b) $\Delta z/R = 0.115$

Table 4: Average percentage change from baseline in low-performance range ($\phi \in [-15^\circ, 15^\circ]$)

		U_∞ (m.s^{-1})			
		5	10	15	20
$\Delta z/R = 0.06$	C_T/σ	−5.8	−6.7	−6.4	−7.3
	C_T/C_P	1.5	0.5	−0.2	−1.8
	C_D	−1.3	−5.6	−7.5	−8.0
$\Delta z/R = 0.115$	C_T/σ	−1.9	−1.9	−0.8	−0.8
	C_T/C_P	3.6	3.5	3.3	2.3
	C_D	1.4	−0.9	−2.6	−3.1

Table 5: Average percentage change from baseline outside low-performance range ($\phi \notin [-15^\circ, 15^\circ]$)

		U_∞ (m.s^{-1})			
		5	10	15	20
$\Delta z/R = 0.06$	C_T/σ	0.7	−0.4	−0.4	−0.9
	C_T/C_P	0.7	0	0.2	−0.1
	C_D	2.3	0.1	0.1	−0.3
$\Delta z/R = 0.115$	C_T/σ	1.3	0.6	1.2	0.9
	C_T/C_P	1.8	1.4	1.9	1.6
	C_D	8.3	3.2	2.5	1.4

line for $\Delta z/R = 0.06$, but remains consistently 2%–4% above baseline for $\Delta z/R = 0.115$. Drag within the low-performance region generally decreases with freestream velocity for both spacings, ranging from −1.3% to −8% for $\Delta z/R = 0.06$, and from +1.4% to −3.1% for $\Delta z/R = 0.115$. Although the rotor used here is not trimmed for lift or propulsive force, the results suggest that in forward flight, a larger axial spacing can achieve performance comparable to a baseline rotor when the blades are closely aligned in azimuth, while smaller spacings perform better at larger azimuthal separations.

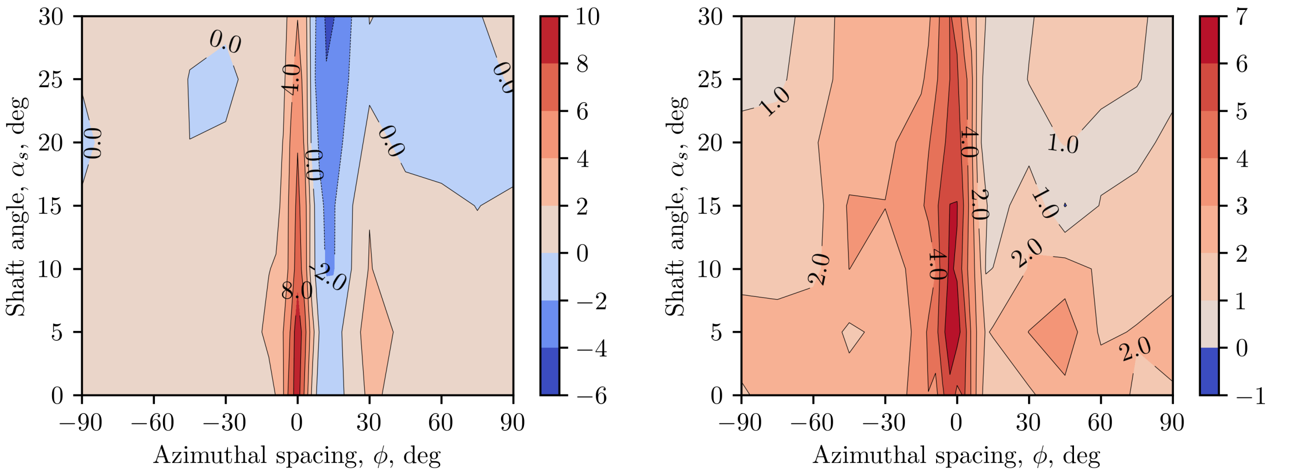

(a) (b)

Figure 12: Percentage change in power loading C_T/C_P relative to the baseline rotor value, plotted against azimuthal spacing ϕ and shaft angle α_s, for a freestream velocity of U_∞ = 5 m.s^{-1} and both axial spacings: (a) $\Delta z/R = 0.06$ (b) $\Delta z/R = 0.115$

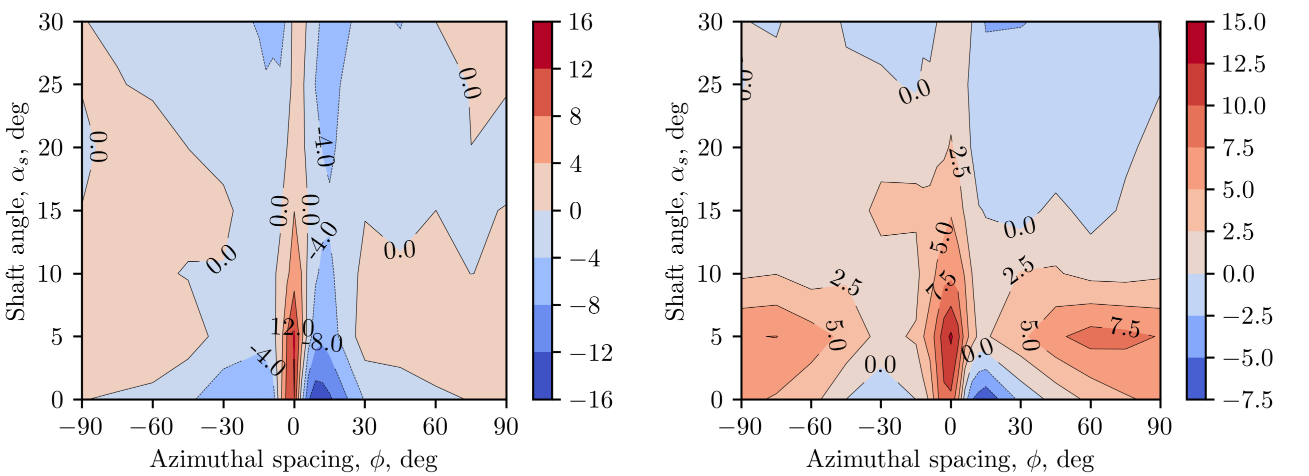

(a) (b)

Figure 13: Percentage change in power loading C_T/C_P relative to the baseline rotor value, plotted against azimuthal spacing ϕ and shaft angle α_s, for a freestream velocity of U_∞ = 20 m.s^{-1} and both axial spacings: (a) $\Delta z/R = 0.06$ (b) $\Delta z/R = 0.115$

CONCLUSIONS

A stacked rotor system comprising two sets of two-bladed rotors was investigated through wind tunnel measurements. The azimuthal spacing, ϕ, was varied across the full range in 15° increments, with a refined resolution of 3° increments between −15° and 15° to capture fine-scale variations near $\phi = 0°$. Two axial spacings were tested, the first, a low axial spacing of $\Delta z/R = 0.06$, represented the smallest possible separation achievable with the current setup without causing physical interference between hubs or blades. At this spacing, strong aerodynamic interactions were expected to have a strong impact on the performance. The second, a high axial spacing of $\Delta z/R = 0.115$, was chosen to reduce interference effects and assess potential performance gains. Comparisons were made against a four-bladed baseline rotor, and the results are presented in three stages: first, the performance of the baseline rotor; second, the hover performance for both axial spacings relative to the baseline; and finally, the forward flight performance, evaluated through blade loading, power loading, and drag coefficient.

- In forward flight, a threshold at a shaft angle of $\alpha_s = 20°$ marks a shift in the dominant velocity component. Below this angle, the in-plane freestream velocity dominates, leading to higher blade loading as U_∞ increases. Above it, the axial inflow becomes dominant, reducing blade loading. The rolling moment depends more strongly on freestream velocity than on shaft angle, while the pitching moment, due to gyroscopic precession, increases with higher freestream velocity and lower shaft angles.
- In hover, the higher axial spacing consistently outperforms the lower spacing at all azimuthal spacings, pro-

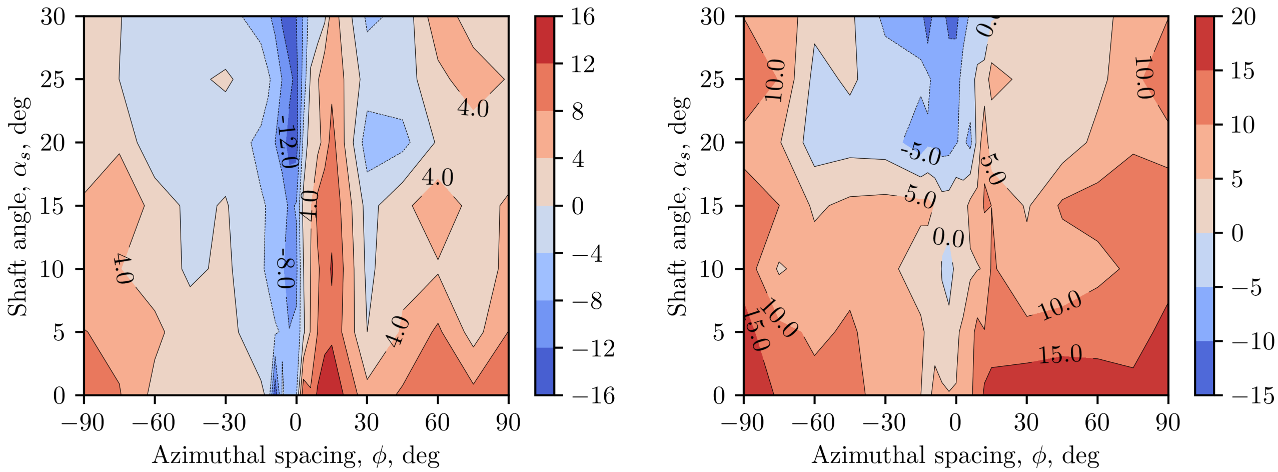

(a) (b)

Figure 14: Percentage change in drag coefficient C_D relative to the baseline rotor value, plotted against azimuthal spacing ϕ and shaft angle α_s, for a freestream velocity of U_∞ = 5 m.s^{-1} and both axial spacings: (a) $\Delta z/R = 0.06$ (b) $\Delta z/R = 0.115$

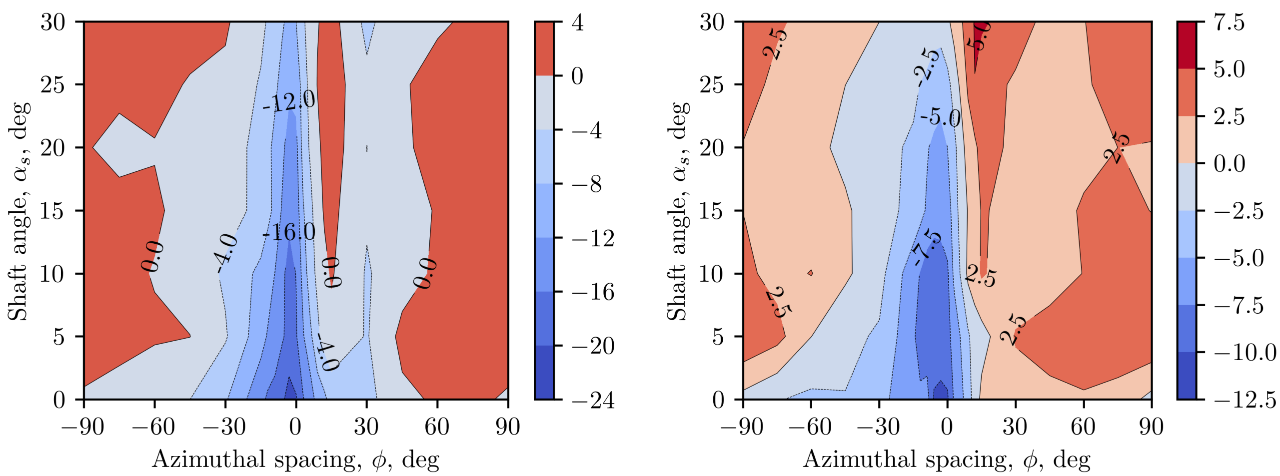

(a) (b)

Figure 15: Percentage change in drag coefficient C_D relative to the baseline rotor value, plotted against azimuthal spacing ϕ and shaft angle α_s, for a freestream velocity of U_∞ = 20 m.s^{-1} and both axial spacings: (a) $\Delta z/R = 0.06$ (b) $\Delta z/R = 0.115$

ducing more thrust and showing smaller fluctuations between maximum and minimum values. Power variation is similar for both spacings except near $\phi = 0°$, where reduced interference at the higher spacing results in smoother and higher average power loading.

- For the low axial spacing, blade loading generally exceeds the baseline except in the range $-15° \leq \phi \leq 15°$, with a peak increase of $+6.61\%$. The high axial spacing surpasses the baseline across all azimuthal spacings, reaching a maximum increase of $+10.26\%$.
- In forward flight, both spacings follow similar trends with azimuthal spacing, but blade loading values are lower relative to the baseline than in hover for all shaft angles and freestream velocities. The high axial spacing maintains higher blade and power loading than the low spacing, while the low spacing generates slightly less drag.
- When compared to the baseline in forward flight, the high axial spacing generally produces more thrust except in the low-performance regions ($-15° \leq \phi \leq 15°$). The low axial spacing shows a broader performance deficit, leading to significantly higher power loading for the high spacing in nearly all configurations. The low spacing power loading values fluctuate around the baseline value except near $\phi = 0°$, where it surpasses it. For both spacings, drag decreases when rotor blades overlap and increases as they separate toward $\phi = \pm 90°$.

AUTHOR CONTACT

Paskal Magier	paskal.magier@usherbrooke.ca
Hachimi Fellouah	hachimi.fellouah@usherbrooke.ca

ACKNOWLEDGMENTS

This work was supported by the Natural Sciences and Engineering Research Council (NSERC) of Canada.

REFERENCES

1. A. J. Landgrebe and E. D. Bellinger, "Experimental investigation of model variable-geometry and OGEE-tip rotors," *Technical Report NASA CR-2275*, Feb. 1974.

2. W. G. O. Sonneborn and J. M. Drees, "The scissors rotor," *Journal of the American Helicopter Society*, vol. 20, pp. 18–27, July 1975.

3. R. Prouty, *Helicopter Aerodynamics - Volume II*. Eagle Eye Solutions, 2009.

4. D. Uehara, J. Sirohi, and M. J. Bhagwat, "Hover performance of corotating and counterrotating coaxial rotors," *Journal of the American Helicopter Society*, vol. 65, Jan. 2019.

5. J. B. Rorke, "Hover performance tests of full scale variable geometry rotors," *Technical Report NASA CR-2713*, Aug. 1976.

6. M. G. Rozhdestvensky, "Scissors rotor concept: New results obtained," in *AHS 52nd Annual Forum, American Helicopter Society*, (Alexandria, VA), pp. 1231–1241, June 1996.

7. G.-H. Xu, S.-C. Wang, and J.-G. Zhao, "Experimental and analytical investigation on aerodynamic characteristics of helicopter scissors tail rotor," *Chinese Journal of Aeronautics*, vol. 14, pp. 193–199, Nov. 2001.

8. D. Uehara and J. Sirohi, "Quantification of swirl recovery in a coaxial rotor system," in *73rd Annual Forum of the American Helicopter Society*, (Fort Worth, TX), May 2017.

9. C. E. Tinney and J. Valdez, "Thrust and acoustic performance of small-scale, coaxial, corotating rotors in hover," *AIAA Journal*, vol. 58, pp. 1–11, Dec. 2019.

10. S. Whiteside, N. Zawodny, X. Fei, N. A. Pettingill, M. D. Patterson, and P. Rothhaar, "An exploration of the performance and acoustic characteristics of UAV-scale stacked rotor configurations," in *AIAA Scitech 2019 Forum*, Jan. 2019.

11. C. Johnson and J. Sirohi, "Experimental measurements and low-order modeling of stacked rotor performance in hover," in *Vertical Flight Society 76th Annual Forum and Technology Display*, Oct. 2020.

12. C. Johnson, J. Sirohi, G. Jacobellis, R. Singh, and R. McDonald, "Investigation stacked rotor performance in hover pt, I: Experimental measurements," in *VFS Transformative Vertical Flight Workshop*, (San Jose, CA), Jan. 2020.

13. G. Jacobellis, R. Singh, C. Johnson, J. Sirohi, and R. McDonald, "Experimental and computational investigation of stacked rotor performance in hover," *Aerospace Science and Technology*, vol. 116, p. 106847, May 2021.

14. C. Johnson, J. Sirohi, G. Jacobellis, and R. Singh, "Performance and acoustics of a stacked rotor with differential collective pitch," *Journal of the American Helicopter Society*, vol. 69, Jan. 2023.

15. R. A. R. Zahirudan, V. T. Valente, E. McThane, A. Hafner, Z. Birkbeck, S. Yan, E. Greenwood, and J. Palacios, "The effect of phase offset angle for coaxial co-rotating rotors," in *Vertical Flight Society 79th Annual Forum and Technology Display*, (West Palm Beach, FL), May 2023.

16. M. Costenoble, J. Baeder, R. Singh, and P. Anusonti-Inthra, "Simulation of airfoil interaction in co-rotating coaxial rotors with uncertainty quantification," in *VFS Transformative Vertical Flight Workshop*, (San Jose, CA, USA), Jan. 2020.

17. J.-S. Park and Y.-B. Lee, "Hover performance analyses of coaxial co-rotating rotors for eVTOL aircraft," *Aerospace*, vol. 9, Mar. 2022.

18. G.-H. Xu, Q.-J. Zhao, and Y.-H. Peng, "Study on the induced velocity and noise characteristics of a scissors rotor," *Journal of Aircraft*, vol. 44, pp. 806–811, May 2007.

19. S. Platzer, M. Hajek, J. Rauleder, P. Mortimer, and J. Sirohi, "Investigation of the flow fields of coaxial stacked and counter-rotating rotors using PIV measurements and URANS simulations," in *Vertical Flight Society 77th Annual Forum and Technology Display*, May 2021.

20. J. A. Valdez and C. E. Tinney, "Wake of a coaxial corotating rotor in hover," *AIAA Journal*, vol. 60, pp. 4829–4839, Aug. 2022.

21. Y. Hong, D. Lee, S. Yang, H. Kook, and K. Yee, "Exploration of stacked rotor designs for aerodynamics in hover," *Aerospace Science and Technology*, vol. 141, p. 108557, Aug. 2023.

22. P. Magier and H. Fellouah, "Experimental investigation of the effect of azimuthal spacing on the performance of a stacked rotor in hover and forward flight," in *Vertical Flight Society 81th Annual Forum and Technology Display*, (Virginia Beach, VA), May 2025.

23. J. G. Leishman, *Principles of Helicopter Aerodynamics*. Cambridge University Press, New York, NY, 2000.

24. W. Johnson, *Rotorcraft Aeromechanics*. Cambridge University Press, New York, NY, 2013.

25. NASA Ames Research Center, C. Russell, J. Jung, G. Willink, and B. Glasner, "Wind Tunnel and Hover Performance Test Results for Multicopter UAS Vehicles," in *Proceedings of the Vertical Flight Society 72nd Annual Forum*, (West Palm Beach, Florida), pp. 1–20, The Vertical Flight Society, May 2016.

26. T. J. Mueller and J. D. DeLaurier, "Aerodynamics of Small Vehicles," *Annual Review of Fluid Mechanics*, vol. 35, pp. 89–111, Jan. 2003.